

1 **Experimental investigation of the brittle-viscous transition in mafic rocks –**
2 **interplay between fracturing, reaction, and viscous deformation**

3

4 **Sina Marti^a, Holger Stünitz^{b,c}, Renée Heilbronner^a, Oliver Plümper^d, Martyn*
5 *Drury^d*

6 ^a Department of Environmental Sciences, Basel University, Switzerland
7 (sina.marti@unibas.ch, +41 79 505 81 82, Brombacherstr. 27, 4057 Basel;
8 renee.heilbronner@unibas.ch)

9 ^b Department of Geosciences, UiT the arctic University of Norway, Norway
10 (holger.stunitz@uit.no)

11 ^c Institut des Sciences de la Terre d'Orléans (ISTO), Université d'Orléans, France

12 ^d Department of Earth Sciences, Utrecht University, Netherlands (O.Plumper@uu.nl;
13 M.R.Drury@uu.nl)

14

15 **Keywords:** Rock deformation experiments, Brittle-viscous transition, Dissolution-
16 precipitation, grain boundary sliding, Polyphase rheology

17

18 **Abstract**

19 Rock deformation experiments are performed on fault gouge fabricated from
20 'Maryland Diabase' rock powder to investigate the transition from dominant brittle
21 to dominant viscous behaviour. At the imposed strain rates of $\dot{\gamma} \sim 3 \cdot 10^{-5} - 3 \cdot 10^{-6} \text{ s}^{-1}$,
22 the transition is observed in the temperature range of ($600 \text{ }^\circ\text{C} < T < 800 \text{ }^\circ\text{C}$) at
23 confining pressures of ($0.5 \text{ GPa} \leq P_c \leq 1.5 \text{ GPa}$). From microstructural observations,
24 the transition is effected by a switch from brittle fracturing and cataclastic flow, to
25 viscous dissolution-precipitation creep and grain boundary sliding. Mineral
26 reactions and resulting grain size refinement by nucleation are observed to be
27 critical processes for the switch to viscous deformation, i.e., grain size sensitive
28 creep. In the transitional regime, the mechanical response of the sample is a mixed-
29 mode between brittle and viscous rheology and microstructures associated with
30 both brittle and viscous deformation are observed. As grain size reduction by
31 reaction and nucleation is a time dependent process, the brittle-viscous transition is
32 not only a function of T but to a large extent also of microstructural evolution.

33

34 **1. Introduction**

35 Our knowledge about rock strength is largely based on laboratory-derived data.
36 Given the condition that the strength of the lithosphere cannot be greater than that
37 of the constituting rocks and minerals, strength envelopes are constructed, which plot
38 laboratory-derived strength or flow laws for minerals (or rocks) versus depth (as a
39 proxy for pressure and temperature) (e.g. Brace and Kohlstedt, 1980; Kohlstedt et
40 al., 1995; Burov, 2011 and references therein). Following the general consensus
41 that the upper crust deforms dominantly by fracturing and the lower crust and
42 upper mantle by viscous creep, the early strength envelopes were constructed
43 using a constant strain rate, two-mechanism model (e.g., Brace and Kohlstedt,
44 1980). Frictional rock strength (Byerlee, 1978) is plotted against depth to
45 temperature and pressure conditions, where viscous deformation takes place at
46 lower stresses than frictional sliding. Here, the term 'viscous' refers to temperature and
47 rate sensitive deformation mechanisms such as dislocation and diffusion creep (including
48 pressure solution creep).

49 Rocks deforming in the brittle field change their mode of deformation from frictional
50 sliding along a discrete plane to distributed cracking at elevated pressures (e.g. Karman,
51 1911; Kirby and Kronenberg, 1984), because frictional sliding at elevated confining
52 pressures requires higher stresses than those needed to form new cracks. This change
53 from discrete to distributed ('ductile') deformation mode is termed "brittle-ductile
54 transition" (BDT) and is also termed the region of semi-brittle deformation (e.g. Kohlstedt
55 et al., 1995). Towards greater depth, the semi-brittle field is terminated by another
56 transition, which is primarily temperature dependent. This transition is termed the
57 "brittle-plastic transition", where the term 'plastic' denotes a permanent, non-brittle
58 deformation without specifying a particular mechanism (Kohlstedt et al. 1995). The term
59 "plastic" may have different meanings in terms of rheology and deformation processes, so
60 that the for a general temperature- and rate sensitive, pressure-insensitive deformation
61 the more general term 'brittle-viscous' transition (BVT) is preferred and will be used in
62 this text. The introduction of a semi-brittle field to the classical strength envelope predicts
63 a broad transitional field from dominant brittle to dominant viscous deformation.

64 The onset of viscous deformation (BVT, or, alternatively, an increasing α -factor for the
65 effective pore pressure law at the BDT, according to Hirth and Beeler, 2015) within the
66 Earth's crust is generally associated with the disappearance of earthquake rupture. Where
67 the occurrence of the BVT is considered to be a simple function of pressure and
68 temperature (as proxies for depth), the BVT regime may be considered as the lower depth

69 limit of the seismogenic zone (e.g. Sibson, 1982, 1984). However, at the BVT several
70 processes are competing: fracturing, frictional sliding, crystal plasticity, and diffusive
71 mass transfer. Given the number of parameters controlling the deformation, the
72 BVT, where both, time-dependent viscous mechanisms and relatively more time-
73 independent brittle and frictional processes significantly contribute to the
74 deformation, is a complex system where temperature, pressure, fluid availability,
75 grain size, strain rate, microstructure, rock composition (i.e. mineral assemblage),
76 and chemical environment control the rheology. As a consequence, it is not
77 surprising that there is a lack of laboratory data characterising the BVT in detail,
78 despite pioneering seminal works by, e.g., e.g., Griggs et al. (1960); Heard (1960);
79 Handin (1966); Byerlee (1967, 1968); Tullis and Yund (1977); Brace and Kohlstedt
80 (1980); Carter and Tsenn (1987); and review in Paterson and Wong (2005) and references
81 therein.

82 In the absence of flow laws for other crustal minerals, the viscous strength of the
83 continental crust was first estimated using a dislocation creep flow law for quartz
84 (Brace and Kohlstedt, 1980). However, large proportions of the lower continental
85 crust, and most of the oceanic crust are of mafic composition and quartz is virtually
86 absent. Strength estimates for these crustal parts could only be assessed since flow
87 law parameters for plagioclase and pyroxene became available (e.g. Mackwell,
88 1991; Raterron and Jaoul, 1991; Bystricky and Mackwell, 2001; Rybacki and
89 Dresen, 2000; Rybacki et al., 2006; Chen et al., 2006; Dimanov et al., 2003;
90 Dimanov and Dresen, 2005; Dimanov et al., 2007). Most of the data, however, is
91 applicable to high temperature deformation, and experimental studies for mafic
92 rocks at lower temperatures are scarce (e.g. Kronenberg and Shelton, 1980;
93 Shelton et al., 1981; Rutter et al., 1985; Hacker and Christire, 1991; Tullis and
94 Yund, 1987; Getsinger and Hirth, 2014).

95 One important aspect of the BVT - not represented in the strength envelope plots -
96 is the development of the rheology of sheared rock over time or during a strain
97 history. Fault- and shear zones may show a strain-dependent microstructural
98 evolution, which, in turn, may cause a strain-dependent strength evolution. One of
99 the consequences of such a strain-history-dependent evolution is that fault/shear
100 zones are unlikely to initiate with their final steady state strength. It is frequently
101 seen from natural examples that brittle and viscous deformation can occur

102 cyclically (e.g. Gratier et al., 2011; Price et al., 2012) or sequentially in time (e.g.
103 Simpson, 1986; Fitz Gerald and Stünitz, 1993; Stünitz and Fitz Gerald, 1993;
104 Trepmann and Stöckert, 2003; Mancktelow and Pennacchioni, 2005; Pennacchioni
105 and Mancktelow, 2007; Fousseis and Handy, 2008; Goncalves et al., 2016; Bukovská
106 et al., 2016).

107 Relatively little is known about the rheology of fault rocks undergoing the BVT. As
108 fault zones are considered to sustain the highest differential stress values near the
109 BVT, it constitutes a key regime controlling the dynamics of lithospheric fault-zone
110 systems. In this study, we aim to further our understanding of the evolution and the
111 rheology of mafic rocks at conditions where the rocks undergo their BVT. Significant
112 amounts of the global seismic moment occur along faults within the oceanic crust
113 and along subduction zones. A better understanding of the behaviour of mafic rocks
114 at the BVT will potentially aid our understanding of earthquake distribution and
115 seismic hazard in these regions.

116 Furthermore, in order to address the question of strain dependent rheology,
117 experiments have been performed to various amounts of strain to observe
118 microstructural changes and evolving mechanical properties during fault-/shear-
119 zone formation. One of the aims of this study is to gain insights into the deformation
120 processes active over the BVT in a mafic rock and how initiation and development
121 of fault/shear zones are achieved. Mechanical response is measured and
122 deformation mechanisms are identified in the brittle, the semi-brittle and the
123 viscous field.

124

125 **2. Methods**

126 *2.1 Experimental procedure*

127 *2.1.1 Sample material*

128 Experiments were performed on Maryland Diabase (Kronenberg and Shelton,
129 1980). The Maryland Diabase starting material ([Table 1](#)) has a modal composition
130 (by volume) of ~ Plagioclase (Pl): 57%, Clinopyroxene (Cpx): 32%, Orthopyroxene
131 (Opx): 8%, accessories (Qz, Kfs, Ilm, Mag, Bt, Ap): 3% (mineral abbreviations after
132 Whitney and Evans, 2010). The Pl shows a relatively homogeneous composition of
133 ~ An₆₅₋₇₀ except for a thin rim with a lower Anorthite component of ~ An₅₀₋₅₅. The
134 core to rim area ratio is ~ 83 : 17 (± 3). Some of the Cpx grains show a Mg-enriched

135 core. Pieces of Maryland diabase were crushed with a hand-press and
136 subsequently crushed with an alumina hand-mortar. The resulting powder was
137 dry-sieved to extract the desired grain size fraction $\leq 125 \mu\text{m}$.

138

139 *2.1.2 Experimental setup and sample assembly*

140 Experiments were performed using two modified Griggs-type deformation
141 apparatus at the University of Tromsø, Norway, at confining pressures (P_c) of
142 $\sim 0.5, 1.0$ and 1.5 GPa , at temperatures (T) of $300, 500, 600, 700$ and $800 \text{ }^\circ\text{C}$ and
143 with constant displacement rates of $\sim 10^{-8}$ to 10^{-9} m s^{-1} (resulting in strain rates of
144 $\sim 3 \cdot 10^{-5}$ to $3 \cdot 10^{-6} \text{ s}^{-1}$ for homogeneous sample deformation). See [Table 2](#) for a list
145 of experiments and conditions.

146 The sample assembly is shown in [Figure 1](#). Solid salt is used as confining medium.
147 Inner salt pieces are fabricated from potassium iodide (KI) for experiments at $T \leq$
148 $600 \text{ }^\circ\text{C}$ and sodium chlorite (NaCl) for experiments at $T \geq 700 \text{ }^\circ\text{C}$. KI is mechanically
149 weaker than NaCl but shows partial melting at $T > 600 \text{ }^\circ\text{C}$ at the pressures of the
150 experiments, which is to be avoided. Outer salt pieces are always fabricated from
151 NaCl.

152 The sample consist of a thin layer of crushed rock, produced by placing 0.11 g of
153 MD powder + $0.2 \mu\text{l H}_2\text{O}$ (equals $0.18 \text{ wt.}\%$) between the Al_2O_3 forcing blocks along
154 a 45° pre-cut ([Figure 1](#)). Forcing blocks are cylindrical with a diameter of 6.33 mm .
155 The sample and forcing blocks are placed in a weld-sealed platinum jacket
156 (0.15 mm wall thickness) with a 0.025 mm nickel foil insert. The amount of added
157 water was chosen such that sufficient water is present for solution mass transport
158 processes and mineral reactions, while not inducing mechanical pore pressure
159 effects. No pore pressure effects in the presence of an aqueous fluid were inferred
160 for contents up to $0.5 \text{ wt } \% \text{ H}_2\text{O}$ by Kronenberg and Tullis (1984) and up to
161 $0.3 \text{ wt}\% \text{ H}_2\text{O}$ by Negrini et al. (2013).

162 During the experiments, approximately 84% of the inelastic axial displacement is
163 accommodated by a shear displacement along the piston-sample interface and
164 approximately 16% by plane strain thinning of the shear zone. The initial shear
165 zone thickness is calculated from the amount of Maryland diabase powder used,
166 the final thickness is measured on thin sections prepared from the samples after
167 the experiment ([Table 2](#)). The shear zone thickness is assumed to decrease linearly

168 throughout the experiment with increasing piston displacement.
169 At higher temperatures, the coupling between forcing blocks and rock material in
170 our experiments was found to be poor. Thus, 800 °C experiments were performed
171 using forcing blocks with 6 regularly spaced grooves, ~ 300 µm wide and 150 µm
172 deep, cut into the surface of both, the upper and lower forcing block.
173 To bring a sample to the desired Pc -T conditions, the σ_1 - and σ_3 -pistons (Figure
174 1) are advanced in small increments, alternated with increments of heating,
175 Heating is achieved using a graphite resistance furnace and T is measured with a K-
176 type thermocouple positioned adjacent to the centre of the shear zone (Figure 1).
177 When the desired conditions are reached (after 5 to 8 h, duration is longer for
178 higher Pc experiments), shear zone thickness is at ~ 0.83 mm. During the
179 experiment, only the σ_1 -piston is advanced. At the end of the experiment, samples
180 are quenched to 200 °C within 2 minutes while simultaneously retreating the σ_1 -
181 piston to remove the load on the sample. After that, samples are brought back to
182 room conditions by slowly removing the remaining load, temperature and Pc,
183 during ~ 3 h.

184

185 *2.2 Derivation of stresses and strains*

186 *2.2.1 Data recording and processing*

187 During the experiment, the confining pressure, axial load, and displacement are
188 recorded using a digital data-logging system (LabView, 7.1) at a sampling
189 frequency of 1 Hz and temperature is monitored using a proportional integral
190 derivative (PID) controller (Eurotherm) attached to the thermocouple.

191 Temperature is held within ± 1 °C by the controller. There is a vertical T gradient in
192 the sample from the center outwards, ranging from ~ 17 °C/mm at 600 °C (Pec,
193 2014).

194 The principal stress σ_3 is considered to be equal to Pc (Eq. 1a), and σ_1 is derived
195 from the measured axial force per sample area.

$$196 \quad \sigma_3 = Pc \quad (1a)$$

$$197 \quad \Delta\sigma = \sigma_1 - \sigma_3 \quad (1b)$$

198

199 $\Delta\sigma$ is corrected for the decreasing overlap of the forcing blocks (i.e. decreasing

200 sample area) using a cosine-square approximation to the ACF.

201

$$202 \quad ac(i) = \cos^2 (90^\circ \cdot sd(i) / L) \quad (2a)$$

$$203 \quad \Delta\sigma_{AC} = ac \cdot \Delta\sigma \quad (2b)$$

204

205 where $ac(i)$: relative overlap of the forcing blocks; $sd(i)$: shear displacement
206 parallel to the forcing block - sample interface; L : maximum possible shear
207 displacement = diameter of forcing blocks (6.33 mm) / $\cos(45^\circ) = 8.95$ mm.

208

209 The shear and normal stresses, τ and σ_n , supported by the sample inclined at 45°
210 are obtained by Mohr circle construction from $\Delta\sigma_{AC}$. The effective pore fluid
211 pressures in our experiments is assumed to be negligible, i.e. is taken as zero.

212 Axial displacement is corrected for apparatus stiffness. Advancing the σ_1 -piston
213 leads to an increased Pc as a function of the compressibility of the confining
214 medium. The correction is outlined in Richter et al. (2016). Differential stress with
215 the solid salt assemblage in the Griggs rig are usually considered to overestimate
216 rock strength eventually up to 100 MPa (e.g. Green & Borch, 1989).

217

218 *2.3 Analytical methods*

219 *2.3.1 Microscopy*

220 After the experiments, samples are impregnated with epoxy, cut parallel to the
221 shear direction (in some cases also normal to it), and prepared to doubly polished
222 thin sections. Optical light microscope, scanning electron microscope (SEM) and
223 transmission electron microscope (TEM) are used for sample analysis. SEM
224 analyses are performed either with the Zeiss Merlin SEM at Tromsø University, or
225 with a Philips XL30 ESEM at the centre of microscopy (SNI) at Basel University.
226 Chemical analyses are performed using energy dispersive X-ray Spectroscopy
227 (EDS), at 15 kV acceleration voltage and using a ZAF matrix correction.

228

229 *Transmission electron microscopy (TEM)* analyses are carried out at Utrecht
230 University using a FEI Talos 200FX equipped with a high-sensitivity Super-EDX
231 system. TEM images are recorded in bright field (BF), high angular annual dark
232 field (HAADF) and bright field scanning TEM (BF-STEM) modes. BF images are

233 highly sensitive on crystallographic orientation, whereas contrasts in HAADF
234 images are sensitive to average atomic number (Z-contrast) of the material.

235

236 *Focussed ion beam (FIB)* foils for TEM investigations are prepared in a FEI Helios
237 NanoLab 3G. The FIB foil of the 600 °C experiment is cut perpendicular to both the
238 shear direction and the shear plane. The FIB foils of the 700 and 800 °C
239 experiments are cut parallel to the shear direction and normal to the shear plane.

240

241 *2.3.2 Image analysis*

242 In this paper, micrographs are always oriented with the shear zone boundaries
243 horizontal and with a dextral sense of shear. The reference coordinate system is
244 shown in [Figure 2](#).

245

246 *FFT analyses of HR-TEM images:* In high-resolution (HR) TEM images where lattice
247 planes of individual crystals are resolved, Fast Fourier Transformations (FFT) can
248 be used to obtain the reciprocal space information akin to a direct diffraction
249 pattern. Lattice fringes are only revealed when the crystal satisfies the diffraction
250 condition. One single HRTEM image of a polycrystalline sample is not likely to
251 reveal lattice fringes in all crystals. Therefore, FFT analysis used to detect
252 diffractions on three HR-TEM images from the same area, with different tilt angles.

253

254 *EDS profiles:* Element concentrations along a line-profile are prepared using the
255 software Fiji (<https://fiji.sc/>). A line-profile of 10 px width is defined, where the
256 value at each point along the profile is an average over these 10 px. In this manner,
257 the noise is reduced. The values are then normalized to the maximum count value
258 (from the whole EDS map) of each element.

259

260 *Phase Segmentation:* Mineral phase segmentations are performed on BSE contrast
261 SEM images. Phases are differentiated by their different Z-contrast using grey-level
262 slicing. As Pyroxene (Px), Amphibole (Amph) and Zoisite (Zo) have similar Z-
263 contrasts, manual post-processing is necessary to properly segment these phases.

264 *Shape and orientation of shear bands:* Shear bands and larger shear fractures are
265 digitized manually on BSE contrast SEM images. The x-y coordinates of the outlines

266 are measured, smoothed (to remove digitizing artefacts) and exported using the
267 program Fiji and analysed with the SURFOR program (Panozzo Heilbronner, 1984;
268 Heilbronner and Barrett, 2014). The SURFOR results yield an orientation
269 distribution function (ODF) of boundary segments of the analysed structures and
270 is presented as a rose diagram. Shear band thicknesses were determined by
271 dividing the digitized shear bands into approximately straight segments, using Fiji
272 to extract the best fit ellipse of each segment and using the short axis of the ellipses
273 as proxy for the shear band thickness.

274 *Grain size and shape:* Grain boundaries are traced manually on SE- and BSE- SEM
275 images or on BF TEM images. The resulting grain maps are analysed with Fiji to
276 derive the grain areas and the x-y coordinates of grain boundaries. The area
277 equivalent diameters are calculated and grain size distributions are presented as
278 histograms of equivalent diameters (d_{equ}). Using a kernel density estimate
279 (MATLAB function 'ksdensity'), the mode of the distribution is determined. Grain
280 shape analyses are performed using the SURFOR program.

281

282 **3. Results**

283 Samples at $T \leq 600$ °C develop similar microstructures and we therefore focus in
284 this paper on the evolution from 600 – 800 °C. Reference frames of image
285 orientation and angles are explained in [Figure 2a, b](#); terminology used when
286 describing stress-strain curves is shown in [Figure 2c](#). Shear strain is always given
287 as apparent shear strain γ_a (for calculation, see Appendix).

288

289 *3.1 Mechanical data*

290 *3.1.1 Stress-strain curves*

291 Shear stress vs. apparent shear strain curves are shown for T of 600 °C, 700 °C and
292 800 °C and P_c of 0.5, 1.0 and 1.5 GPa ([Figure 3a](#)). Samples at 600 and 700 °C show a
293 positive dependence of τ on P_c between 0.5 and 1.0 GPa.

294 The comparison of the stress-strain data for 700 °C experiments between 1.0 and
295 1.5 GPa P_c shows that the yield point occurs at relatively similar values. The 1.5
296 GPa P_c experiments however, unlike all other experiments, show hardening at 700
297 °C until $\gamma_a \sim 2.3$ where stresses stay at approximately constant levels thereafter.

298 At 800 °C, sample strength is significantly lower than in lower T experiments and
 299 within the variability between individual runs, no strength dependence on Pc is
 300 detected. 800 °C experiments show a gradual weakening after peak stress and
 301 reach a quasi-steady state at a $\gamma_a \sim 4$ onwards (Figure 3a). Note also the lower
 302 slope of the initial loading part of the stress-strain curve at 800 °C compared to
 303 lower T experiments. Samples at 800 °C deform at stresses below the Goetze
 304 criterion (the condition of $\Delta \sigma = Pc$, which is taken as the upper $\Delta \sigma$ -limit of
 305 plastic or viscous deformation; Kohlstedt, 1995. In our samples, which are oriented
 306 at 45° to σ_1 , $\Delta \sigma = 2 \cdot \tau$). At lower temperatures, all sample deform at $\Delta \sigma$
 307 clearly above the Goetze criterion.

308

309 3.1.2 Mohr Circle construction

310 From Mohr circle constructions (Figure 3b), the positive pressure dependence of
 311 strength at 600 °C is clearly visible. Apparent friction coefficients (μ') derived from
 312 the Mohr circles yield a value of $\mu' = 0.44$. Experiments at 600 °C and 700 °C, 0.5
 313 GPa Pc reach Byerlee's relationship (Byerlee, 1978) at 'yield', whereas at 1.0 GPa,
 314 the stresses at both 'yield' and flow stay below it. At $Pc \geq 1.0$ GPa, and $T \geq 700$ °C,
 315 shear stresses are pressure insensitive with an apparent friction coefficient of $\mu' =$
 316 0.05 at 700 °C. No " μ " was determined for 800 °C experiments, due to the
 317 variability in the stress values and the sensitivity of the fitted " μ " to low slopes.
 318 However, whereas 'yield' stresses do not show any significant pressure
 319 dependence, quasi-steady state values reach lower values in the lower Pc
 320 experiments at 800 °C.

321

322 3.1.3 Stress exponents

323 Combining constant displacement rate and displacement rate stepping tests, a
 324 stress exponent n is determined as

325

$$326 \quad \tau \propto \dot{\gamma}^{1/n} \quad (3)$$

327

328 where τ : shear stress and $\dot{\gamma}$: shear strain rate. To assess the influence of different
 329 data correction routines on calculated stress exponents n , some of our data is

330 calculated with different published correction routines, to show their influence on
331 the determined stress exponents. The corrections compared are:

332 1) 'R16': Data correction described in Richter et al. (2016). The same procedure for
333 stress calculations is followed in this paper .

334 2) 'R16 + H&K10': Data correction after Richter et al. (2016) with the stress
335 correction for the solid-salt assembly after Holyoke III and Kronenberg (2010).

336 3) 'P12': Data correction described in Pec et al. (2012).

337 4) 'P12 + H&K10': Data correction after (Pec et al., 2012) with the stress correction
338 for the solid-salt assembly after (Holyoke III and Kronenberg, 2010).

339

340 n values are determined for experiments performed at $T = 300\text{ °C}$, $P_c = 0.5\text{ GPa}$; T
341 $= 500\text{ °C}$, $P_c = 1.0\text{ GPa}$; $T = 700\text{ °C}$, $P_c = 1.0\text{ GPa}$ and $T = 800\text{ °C}$, $P_c = 1.0\text{ GPa}$ (Figure
342 4). For $T \leq 500\text{ °C}$ n is large with values > 19 , n for 700 °C experiments is
343 significantly lower with a value of 5.6 and n at 800 °C is as low as 1.9. The n values
344 determined from different data correction conventions from the literature vary by
345 16 – 27% (Figure 4b). For example for the $T = 800\text{ °C}$, $P_c = 1.0\text{ GPa}$ experiments, a
346 range of n values from 1.6 – 1.9 arises from different data treatment routines.

347

348 *3.2 Microstructures*

349 *3.2.1 Overview*

350 Strain in experiments at all P_c - T conditions localizes into a network of shear
351 fractures and/or shear bands. The term 'shear band' is used to refer to a zone (with
352 a certain thickness) of high strain accumulation, without any implication of a
353 specific deformation mechanism. As opposite to a 'shear fracture', which is
354 accommodating displacement along a plane without any obvious distribution of
355 strain within a volume (at SEM resolution).

356 The microstructures developed at different temperatures are systematically
357 different (Figure 5). At 600 °C , the microstructure is dominated by brittle
358 deformation. Fracturing is extensive and a foliation (S), defined by elongated
359 aggregate shapes, develops due to cataclastic flow (Figure 5a, b). Larger shear
360 displacements are accommodated along shear fractures and shear bands, usually
361 in Riedel shear (R_1) orientation. Grain size reduction occurs via pervasive micro-
362 fracturing (Figure 5b). No obvious strength difference between Pl and Px is

363 observed, as interpreted from the similar degree of fracturing and aggregate
364 elongation of the two phases. In rare occasions, delicate pore trails are seen where
365 fractures are partially healed, potentially indicating limited solution mass transfer
366 (Figure 5c).

367 The microstructures in 700 °C experiments are discussed for the case of $P_c = 1.0$
368 and 1.5 GPa. At 700 °C, fracturing of (especially Px-) porphyroclasts is still
369 observed and a weak foliation (defined by elongated aggregate shapes) forms
370 partly by cataclastic flow (Figure 5d). Strain is localized in a network of thin (~ 5 –
371 15 μm wide) shear bands in C' orientations, cross-cutting the foliation (Figure 5d,
372 e). These shear bands consist of small ($\ll 1 \mu\text{m}$) grains of mainly Pl, Amph and Zo
373 (Figure 5e). Amph and Zo are not part of the starting material and represent syn-
374 kinematic reaction products. The reaction to Amph occurs preferentially along
375 zones of localized deformation such as fractures within Px clasts and along shear
376 bands (Figure 6). The reaction to Zo and more albitic Pl occurs throughout the
377 samples, but small Zo needles predominantly occur in shear bands. Both, the Amph
378 and Zo forming reactions are observed at $P_c = 1.0$ and 1.5 GPa, but occur more
379 extensively at 1.5 GPa.

380 At 800 °C broad shear bands form, separating low strain lenses between them
381 (Figure 5f). Shear bands are recognized by small grain sizes and a fine-scale
382 compositional layering defining a foliation (Figure 5g). Fracturing is only minor
383 represented in the microstructure but can still be observed. Mineral reactions
384 occur pervasively throughout the sample (i.e. are not restricted to high strain
385 zones) but are more abundant in shear bands compared to low strain lenses. Amph
386 either grows as coronas around Px grains or as aggregates within shear bands
387 (Figure 5g) and has a composition between Mg-Hornblende to Tschermakite
388 (Amph classification after Hawthorne et al., 2012). Zo grains occur as small needles
389 within Pl clasts or within shear bands. Grain sizes in shear bands are usually < 1
390 μm . Experiments at 800 °C and 1.5 GPa P_c show very similar microstructures but
391 the Amph and especially Zo reaction are more abundant at the higher P_c
392 conditions.

393 Some melting is observed at 800 °C (melt vol.-% of total sample vol. ≤ 2), where the
394 melt is mainly seen to form small pockets situated in extensional sites between
395 larger porphyroclasts. No melt bands or shear-parallel melt layers are observed.

396 The geometry of strain localization changes over the temperature range from 600
397 – 800 °C (Figure 7). Shear bands and shear fractures at 600 °C tend to be few, with
398 large displacements. At 700 °C, shear bands are more abundant, shorter and more
399 anastomosing compared to the lower T experiments. Fractures with larger
400 displacements are less abundant but still observed. At 800 °C, shear bands are
401 broad and form an anastomosing network. Generally no shear fractures with any
402 significant amount of displacement are observed at 800 °C. The preferred
403 orientations of shear bands and shear fractures with respect to the load axis
404 increases from 30° at 600 °C (or 15° towards the shear zone boundaries) to 42° at
405 800 °C (or 3° towards the shear zone boundaries; Figure 7).

406

407 *3.2.2 Shear bands formed in low T experiments*

408 Shear bands at 600 °C usually have a thickness of ~2 to 10 µm (Figure 7b) and
409 occur both, along parts of the sample-forcing block interface and traversing the
410 sample. The shear bands are either formed by ultra-cataclasites (type-I shear
411 bands) or by a material that shows flow structures, seen by perturbation of a
412 micron- to sub-micron scale compositional layering (type II shear bands) (Figure
413 8a). There is a clear and relatively abrupt grain size gradient over a few microns
414 from the lower strain areas into the type-II shear bands. Whereas the material in
415 the low strain domains is usually pervasively fractured, no fractures or grain
416 fragments are resolved within shear bands (at SEM resolution). A type II shear
417 band as shown in Figure 8a has been studied in more detail by TEM. The material
418 in the lower strain domains that border the shear bands consists of larger (>>100
419 nm) angular Pl fragments and the boundary to the shear band material is sharp
420 (Figure 8b). The shear band itself is composed of nano-crystalline and amorphous
421 material in lenticular aggregates and layers, both with fairly sharp boundaries.
422 Some crystals, identifiable by their darker appearance due to diffraction, are
423 observed within the amorphous layers (Figure 8b - d). Lattice planes, seen in high-
424 resolution BF HRTEM images and detected in FFT images show that the
425 amorphously appearing layers still contain nano-crystals (Figure 8d).

426

427 *3.2.3 Shear bands formed in intermediate T experiments*

428 [Figure 9](#) presents microstructures from shear bands developed at 700°C, 1.0GPa
429 Pc. At these 700 °C and Pc of 1.0 and 1.5 GPa conditions, shear bands are fully
430 crystalline and mainly composed of fine-grained Pl and Amph ([Figure 9c](#)). Pl grain
431 sizes are on the order of ~100 – 200 nm ([Figure 9b](#); [12](#)). [Figure 9e](#) shows the result
432 of TEM EDS analysis over an area containing a small Pl porphyroclast surrounded
433 by fine-grained Pl in the shear band. Plotting the relative amounts of the elements
434 Si, Ca and Al along a profile from the porphyroclast into the fine-grained matrix
435 shows slightly higher Al and Ca contents and lower Si content in the porphyroclast
436 compared to the Pl within the shear band.

437

438 *3.2.4 Shear bands formed in high T experiments*

439 Shear bands formed at 800 °C (Pc = 1.0 and 1.5 GPa) are fully crystalline. The
440 typical microstructure shows fine-grained Pl interlayered with Amph (+Qz)
441 ([Figure 10a, c](#)) and a close-up on the Pl grains shows ‘diamond shaped’, largely
442 defect-free grains with a weak shape preferred orientation ([Figure 10b](#); [11](#)). The
443 mean axial ratio of grains is $b/a = 0.64$ and grain sizes are on the order of ~ 0.15 –
444 0.50 μm ([Figure 12](#)). Pore space along grain boundaries is almost absent and grain
445 boundaries are tight ([Figure 10b](#); [11a](#)). Pl grain boundaries show a strong
446 preferred orientation in two maxima ~ 10 – 30° away from the shear plane in both
447 directions ([Figure 11](#)). Aligned grain boundaries are frequently observed, where
448 relatively straight grain boundaries can be traced continuous over several
449 neighbouring grains ([Figure 11c](#)). The ODF of grain boundary segments is weakly
450 anisotropic with a monoclinic shape, consistent with the global dextral sense of
451 shear.

452

453 *3.2.5 Grain size distribution of plagioclase in shear bands formed in 700 – 800 °C* 454 *experiments*

455 [Figure 12](#) presents grain size distributions (GSD) measured from Pl grains within
456 shear bands formed at 700 and 800 °C. Due to the small grain sizes in shear bands
457 at 700 °C, it is difficult to distinguish individual grains. The best results were
458 obtained from SE SEM images of broken surface as shown in [Figure 9b](#). For the 800
459 °C experiments, grain maps were produced from both TEM and SEM images. Size
460 distributions obtained from TEM and SEM images are similar and the GSD

461 presented in [Figure 12b](#) is measured on Pl grains from TEM images (similar to
462 those shown in [Figure 10](#)). The GSD in [Figure 12a](#) is measured from grains
463 segmented on SEM images of broken surfaces of a shear band top-view ([Figure 9b](#)),
464 thus from a quasi-3D view, whereas the GSD in [Figure 12b](#) is from the 2D section of
465 grains measured from a FIB foil in the TEM. Consequently, the two GSD are not
466 fully comparable but yield a semi-quantitative measure of the grain size
467 differences in shear bands between 700 and 800 °C experiments. The size
468 distribution developed at 700 °C is narrow and > 80% of all grains are within 0.11
469 – 0.25 µm. The mode of the calculated kernel density estimate fit lies at 0.17 µm.
470 The GSD at 800 °C is somewhat broader and > 80% of all grains are within 0.15 –
471 0.50 µm with a mode of the kernel density estimate calculated fit at 0.30 µm.

472

473 *3.2.6 Shear band evolution with strain in 800 °C experiments*

474 [Figure 13](#) presents the evolution of shear bands at 800°C, as observed from
475 experiments performed to different amounts of bulk strain, from peak stress ($\gamma_a \sim$
476 0.7) to a max of $\gamma_a \sim 6.8$. At peak stress, initial shear localization occurs mainly
477 along favourably oriented grain- and phase boundaries. These initial zones are
478 short ($\sim 100 - 200 \mu\text{m}$), distributed (not interconnected) and make an angle of
479 $\sim 27^\circ$ with the load axis. From the microstructure it is apparent that these
480 structures are often dilatant: minor melt segregations, microfracturing and
481 nucleation of new grains/phases such as Amph and Pl are observed ([Figure 14](#)).
482 With increasing strain, the initial shear bands start to connect by the formation of
483 interconnected zones of fine-grained material. These zones make a smaller angle to
484 the shear zone boundaries (or $\sim 39^\circ$ with respect to the load axis) and have a
485 width of $\sim 10 - 20 \mu\text{m}$. At a shear strain of $\gamma_a \sim 4$, a network of anastomosing
486 shear bands has formed, with $\sim 3^\circ$ with respect to the shear zone boundaries (i.e.
487 42° to the load axis). The main shear band strand has a thickness of 50 – 150 µm.
488 This microstructure coincides with the attainment of a quasi-steady state in the
489 mechanical data ([Figure 13a, b](#)). With increasing strain, the vol.-% of shear bands
490 increases. Irrespective, sample strength varies only slightly between $\gamma_a \sim 4$ to 6.8
491 despite the significant increase in vol.-% of shear bands ([Figure 13b, c](#)).

492

493 *3.2.7 Shear band orientation from peak stress to higher strains*

494 **Figure 15** shows the difference of shear band orientation at peak stress
495 (~ coinciding with initiation of localization) and at higher strains (at quasi-steady
496 state), as a function of temperature. Initial shear bands at all temperatures show
497 the same preferred orientation, with 27° towards the load axis. This orientation
498 stays relatively constant at ~ 30° in 600 °C experiment, but angles increase to 33°
499 at 700 °C and 42° at 800 °C.

500

501 **4. Discussion**

502 The strains attained in our experiments are insufficient to attain full
503 microstructural steady state. However, it is expected that the mechanical data
504 reaches quasi-steady state values. The inferred rheology of the samples (e.g. as
505 approximated by the determined stress exponents) always represents a bulk
506 sample rheology, caused by combined mechanisms of deformation and their
507 different rates in low strain domains and shear bands.

508

509 *4.1 Deformation mechanisms*

510 *4.1.1 low T experiments*

511 At 600 °C, displacement is mainly accommodated by cataclastic flow. The
512 mechanical data shows a clear positive dependence of sample strength on P_c
513 (**Figure 3a, b**). High n values of ~20 (**Figure 4**) are in accordance with dominant
514 brittle deformation and frictional sliding, as it is observed from the microstructure
515 (**Figure 5b**). Some viscous component of deformation may be indicated by the fact
516 that the n values are not as high as could be expected for purely frictional
517 behaviour.

518 Displacement in 600 °C experiments is localized in a network of shear fractures
519 and fine-grained shear bands (**Figure 5a, b; 7**), some of which contain amorphous
520 material (**Figure 8**). The angles of shear bands and shear fractures to the load axis
521 (~27° - 30°, **Figure 15**) are in accordance with brittle Riedel (R_1) structures.

522 The area-% of shear bands in the thin section is about 1 – 2%. As an upper-bound
523 estimate, if all displacement were to be accommodated by the shear bands, the
524 strain rate $\dot{\gamma}$ within them would be on the order of

525

526 $\dot{\gamma} = 10^{-5} \text{ mm s}^{-1} / (0.64 \text{ mm} \cdot 0.02) \approx 8 \cdot 10^{-4} \text{ s}^{-1}$ (3)

527

528 which is the applied displacement rate divided by 2% of the approximate shear
529 zone thickness. Although the strain rate within the shear bands is likely to be high,
530 it stays well below seismic rates.

531 Partly amorphous shear bands as we observe them during aseismic brittle faulting
532 have previously been described (e.g. Yund et al., 1990; Goldsby and Tullis, 2002;
533 Janssen et al., 2010; Pec et al., 2012, 2016). Our TEM analyses show that the shear
534 bands consist of amorphous material, with layers and lenses of nano-crystalline
535 material (Figure 8). A clear material difference is seen between Pl and Px, where Pl
536 preferentially becomes amorphous and Px remains largely crystalline, with very
537 small sizes (< 50 nm, Figure 8c). This is similar to the results of Pec et al. (2012,
538 2016) or Yund et al. (1990): In their granitoid sample material amorphous shear
539 bands form extensively within the feldspatic material.

540 The boundaries between shear bands and host rock in our samples are sharp, even
541 on the nano-scale (Figure 8b). It appears from the microstructure that crystalline
542 material is comminuted to a certain grain size (< 50 nm) and below that,
543 amorphization (mainly of the Pl) is effective. (Pec et al., 2012, 2016) discuss
544 different possible formation mechanism for their amorphous material and
545 conclude that the most likely mechanism is a type of mechanical amorphization, i.e.
546 high defect densities until crystallinity is lost. Feldspars appear to be particularly
547 susceptible to this process, as also supported by this study. The rheology of these
548 (partly-)amorphous shear bands, however remains yet unclear.

549

550 *4.1.2 High T experiments*

551 At 800 °C, there is a significant difference in rheology compared to lower T
552 experiments: differential stresses at 800 °C are half as high as at 700 °C and stay
553 always below the Goetze criterion (Table 2; Figure 3a). Initial stress increase
554 during sample loading (before peak stress) shows lower slopes at 800 °C (Figure
555 3a), indicating a larger component of viscous deformation early in the experiment.
556 The microstructure at 800 °C is dominated by mineral reactions and strong grain
557 size refinement (Figure 5f, g; 10). The grain size within shear bands ranges mainly
558 between 0.15 – 0.50 µm for Pl (Figure 12b), with similar sizes for Amph and Zo.

559 Grain size reduction takes place mainly by nucleation of new grains in conjunction
560 with mineral reactions and potentially aided by strain energy reduction by
561 replacing old, defect-rich porphyroclasts by new defect-free grains. The small grain
562 sizes facilitate a grain size sensitive creep mechanism, where the strain rate is
563 proportional to d^{-m} (e.g. Ashby and Verrall, 1973; Coble, 1963; Rutter, 1976), where
564 d is the grain size and m the grain size exponent. Diffusion creep and grain
565 boundary sliding (GBS) are known to only leave few microstructural traces of their
566 activity. However, aligned grain boundaries, equant to weakly anisotropic grain
567 shapes, and low internal defect densities of grains are microstructures
568 characteristic for GBS and diffusion creep (e.g. Elliott, 1973; Boullier and Gueguen,
569 1975; Gifkins, 1976; Drury and Humphreys, 1988; Kilian et al., 2011; Drury et al.,
570 2011). The shear bands consist of small, elongated hexagonal grains, whose grain
571 boundaries can be contiguous over several grain diameters (Figure 11). The
572 contiguous grain boundaries are well orientated for sliding in all orientations. As
573 the experiments are performed with H₂O present, dissolution-precipitation creep
574 (DPC) is interpreted to be the dominant form of diffusion creep.
575 DPC needs to be accommodated by some GBS (Lifshitz sliding of Langdon 2006),
576 but the main strain contribution in very small sized aggregates may take place by
577 GBS, where diffusive mass transport accommodates shape changes (Rachinger
578 sliding of Langdon 2006). As both processes are closely linked and interconnected,
579 the term DPC includes both, diffusion creep and GBS.
580 DPC as a dominant deformation mechanism is in accordance with the low observed
581 stress exponents of $n \sim 1.9$. Usually, stress exponents for diffusion creep are
582 expected to be close or equal to 1 (e.g. Ashby and Verrall, 1973; Coble, 1963;
583 Karato, 2008, Kohlstedt and Hansen, 2015; Paterson, 2013), but higher n values
584 have been suggested for DPC, depending on the driving potentials or chemical
585 potential gradients along the grain contact area (e.g., Gratier et al. 2009, 2013). In
586 low strain domains grain sizes are large and DPC will not be an efficient
587 deformation mechanism in these. Frictional sliding may be active in the low strain
588 domains (but not dominant), increasing the stress exponent of the bulk sample to n
589 = 1.9. Diffusion creep as viscous deformation mechanism has previously been
590 suggested for experimentally deformed basaltic material (under water added
591 conditions) by e.g. Rutter et al. (1985); Getsinger and Hirth (2014), whereas Rutter

592 et al. (1985) state more in detail, that they interpret DPC together with GBS to be
593 the dominant deformation mechanism.

594

595 *4.1.3 Intermediate temperature experiments*

596 The microstructure at 700 °C shows characteristics of both DPC (including GBS)
597 and cataclastic flow. Cataclastic flow thereby is mainly observed to contribute to
598 deformation in low strain lenses (Figure 5d; 6). In shear bands, the similar
599 microstructures as in shear bands at 800 °C suggest that DPC is the dominant
600 deformation mechanisms in shear bands at 700 °C too. The main difference
601 between 800 and 700 °C is the somewhat smaller grain sizes in shear bands at 700
602 °C (Figure 12).

603 Fracturing at 700 °C is subordinate within shear bands. Fracturing and cataclasis
604 are expected to produce a wide range of grain sizes with angular grain shapes (e.g.
605 Stel, 1981; Storti et al., 2003; Keulen et al., 2007), unlike the observed
606 microstructure. TEM-EDS mapping also reveals a compositional difference
607 between Pl porphyroclast and fine-grained shear band Pl (Figure 9), which is
608 further evidence that the plagioclase grains within the shear bands are not a result
609 of fracturing but rather result from neocrystallization. The chemical differences are
610 small but the coupled Al+Ca decrease with a Si increase from the clast to the shear
611 band is consistent with a change towards lower anorthite content in the matrix Pl
612 of the shear band. The measured change in Pl chemistry between porphyroclasts
613 and fine-grained shear band Pl also excludes subgrain rotation recrystallization
614 and instead points to nucleation as means of grain size reduction.

615 However, a brittle precursor to the shear bands at 700°C is possible, interpreted
616 from the initiation of shear bands with the same low angle towards the load axis as
617 in the brittle dominated 600°C experiments (Figure 15), as well as by the similar
618 sample strengths for 600 and 700°C experiments. Due to the low strains at shear
619 band initiation (~ at peak stress) it is, however, difficult to identify from the
620 microstructure if and in which proportions viscous or brittle processes contribute
621 at the point of initiating strain localization.

622 At 700 °C, sample strength as seen from the stress-strain curves is comparable to
623 the 600 °C experiments (Figure 3a) with a significantly lower stress sensitivity on
624 strain rate ($1/n$) ($n = 5.6$ at 700 °C, $n > 19$ at $T < 600$ °C; Figure 4a). The stress

625 exponent of 5.6 is just slightly higher than what would be typical for dislocation
626 creep ($n = 3$ to 5 ; Karato, 2008; Paterson, 2013; Kohlstedt and Hansen, 2015), but
627 none of the microstructures indicate evidence for crystal plasticity. Rather, the
628 intermediate n -value is interpreted to result from a combination of predominantly
629 brittle (n -values of 19.5 and higher) and viscous processes ($n \sim 1.9$), as it is
630 observed in the microstructure.

631

632 *4.1.4 Summary of deformation mechanisms*

633 The dominance of viscous deformation at 800 °C, and of brittle deformation at 600
634 °C is evident, both from the mechanical data and the microstructure. Samples
635 deformed at 700 °C are an intermediate case, where strain is localized into shear
636 bands which are interpreted to deform with a viscous deformation mechanism but
637 with stress-strain curves and strengths more like the brittle-dominated 600 °C
638 samples (Figure 3a).

639 Shear bands formed in 700 °C experiments, like the shear bands at 800 °C, are
640 interpreted to accommodate strain mainly by DPC and GBS. However, low strain
641 lenses at 700 °C show abundant microfracturing and a contribution of cataclastic
642 flow to deformation. The stress exponent is considerably lower at 700 °C than for
643 lower T experiments (Figure 4a), indicating an increased viscous component to the
644 rheology at 700 °C. The stress exponent of $n = 5.6$ for 700 °C experiments is
645 interpreted as a mixed mechanical response determined by the rheology of
646 viscously deforming shear bands and partly frictional/cataclastic low strain lenses.
647 The transition from dominantly brittle deformation to dominantly viscous flow in
648 our experiments is seen to initiate with the dominance of solution-mass transport.
649 Mineral reactions and nucleation lead to grain size reduction and thus strongly
650 enhance the strain rate of grain size sensitive creep mechanisms. For our imposed
651 experimental displacement rates, the transition occurs around 700 °C (although
652 not fully P_c insensitive). In deformation experiments on whole-rock cores of
653 Maryland Diabase at conditions similar to ours, Kronenberg and Shelton (1980)
654 observed a brittle-viscous transition in their samples around 700 °C for a $P_c = 1.0$
655 GPa, comparable to our observations. However their strain rate was approximately
656 one order of magnitude lower.

657 In our experiments, the influence of Pc is less pronounced compared to that of the
658 temperature. Increasing the Pc at, e.g., 600 °C does not lead to a transition to more
659 viscous behaviour. At 700 and 800 °C, the main effect of increasing the Pc is the
660 formation of a higher abundance of reaction products. This indicates a rate-
661 enhancing effect of increasing Pc on solution-mass transport processes and/or
662 reaction kinetics, e.g., by a greater overstepping of reaction boundaries for
663 pressure sensitive reactions.

664

665 *4.2 Microstructural evolution and its influence on bulk rheology*

666 *4.2.1 Shear band evolution*

667 As seen from 800 °C experiments, shear bands are widening and increase in vol.-%
668 with increasing strain ([Figure 13](#)), caused by the on-going process of mineral
669 reactions and nucleation, leading to the replacement of old, coarser-grained
670 porphyroclasts by new, sub-micron sized grains. Shear band vol.-% stays relatively
671 low in 700 °C experiments for the strains achieved, and interconnectivity is much
672 lower than at 800°C (e.g. [Figure 7](#)). From the mechanical data it is seen that 700 °C
673 experiments still show a large influence of brittle deformation, which is attributed
674 to the low volume percentage, unfavourable orientation (not parallel to shear zone
675 boundary but inclined against it with $\sim 7^\circ$), and poor interconnectivity of shear
676 bands. With increasing shear band widening, the viscous rheology of the shear
677 bands at 700 °C is expected to eventually become more dominant.

678 As reaction and diffusion rates are lower at lower T, more time (or equivalently
679 strain) is needed in the case of the 700 °C experiment to attain a connected
680 network of shear bands as it is observed at 800 °C. However, the positive feedback
681 between fracturing and reaction kinetics (as seen from extensive mineral reactions
682 along microfractures in 700 °C experiments, [Figure 6](#)) aids the microstructural
683 change, i.e. grain size reduction by reaction and nucleation, and appears to be an
684 important mechanism in switching from dominant brittle to more viscous
685 rheology.

686 Comparing the orientations of shear bands formed at different T ([Figure 7](#)) it is
687 apparent that the orientations are less favourable for bulk shear displacement in
688 600 and 700 °C compared to 800 °C experiments, due to the higher inclination of
689 shear bands to the shear zone boundaries. Thus, shear band orientation is an

690 additional factor determining how the weak phase controls the rheology (cf. Gerbi
691 et al., 2016).

692

693 *4.2.2. Shear band influence on bulk rheology in high-T experiments – estimating flow*
694 *stresses in shear bands from plagioclase diffusion creep flow law*

695 The shear band evolution in 800 °C experiments shows an increasing dominance in
696 shear band orientations (sub-)parallel to the shear zone boundaries (Figure 13)
697 with increasing shear band widening and interconnection. That is, the shear band
698 network evolves into geometrically more favourable orientations. Sample
699 strengths, however, remain relatively high, with shear stress values of $\tau > 190\text{MPa}$
700 (Table 2; Figure 3a). Additionally, a quasi-steady state in the stress-strain curves at
701 $\gamma_a \gtrsim 4$ is reached, disregarding a still increasing shear band vol.-%. These
702 observations again suggest that the bulk sample rheology is not simply determined
703 by the rheology of the shear bands.

704 For our experimental samples, the imposed displacement rate, temperature and
705 the grain size within shear bands are known. At 800°C, where dissolution
706 precipitation creep is interpreted to dominate the deformation, we can attempt to
707 calculate expected stresses within shear bands for the given conditions. At present,
708 however, the lack of, e.g., mineral solubility data and properties of grain boundary
709 fluid films does not allow to calculate strain rates from common dissolution
710 precipitation creep flow laws at the elevated Pc/T conditions of our experiments.
711 We use a simplified approach to estimate the shear band rheology by applying the
712 flow law of Rybacki and Dresen (2000) (shortened as ‘RD00’) for diffusion creep in
713 feldspars, as has been done previously by e.g. Getsinger and Hirth (2014). The flow
714 law of RD00 has the form:

715

$$716 \quad \dot{\epsilon} = A \cdot \Delta\sigma^n \cdot d^{-m} \cdot \exp\left(-\frac{Q}{RT}\right) \quad (5)$$

717

718 where A : constant, $\Delta\sigma$: differential stress, n : stress exponent (usually ~ 1), d :
719 grain size, m : grain size exponent, Q : activation energy, R : universal gas constant,
720 T : temperature.

721 Under the assumption that the shear bands accommodate the majority of the
722 deformation, a shear strain rate of $\sim 1 \times 10^{-4} \text{ s}^{-1}$ is assumed for them. This is
723 derived from the imposed displacement rate, $\sim 1 \times 10^{-5} \text{ mm s}^{-1}$ divided by the
724 cumulative shear band thickness, $\sim 8 \times 10^{-2} \text{ mm}$ (which is 10 – 20% of the total
725 sample thickness at quasi-steady state in the mechanical data, e.g. [Figure 13](#)).
726 Using the RD00 flow law for diffusion creep in a wet plagioclase aggregate, we use
727 a strain rate of $1 \times 10^{-4} \text{ s}^{-1}$, a grain size range of 0.15 – 0.50 μm and $T = 800 \text{ }^\circ\text{C}$. To
728 compare our shear strain rates to the axial shortening strain rates of the flow law,
729 the conversion from axial shortening to simple shear strain rates after Schmid et al.
730 (1987) is used, reformulating Eq. (5) to :

731

$$732 \quad \dot{\gamma} = A \cdot \sqrt{3}^{(n+1)} \cdot \tau^n \cdot d^{-m} \cdot \exp\left(-\frac{Q}{RT}\right) \quad (6)$$

733 $\dot{\gamma}$: shear strain rate, A : constant, n : stress exponent = 1, τ : shear stress, d : grain
734 size, m : grain size exponent = 3, Q : activation energy, R : universal gas constant, T :
735 temperature.

736

737 Solving Eq. (6) for shear stresses, they are calculated as:

$$738 \quad \tau = \exp\left(\log\left(\frac{\dot{\gamma}}{A \cdot \sqrt{3}^{(n+1)} \cdot d^{-m}}\right) - \left(\frac{-Q}{R \cdot T}\right)\right) \quad (7)$$

739

740 Resulting shear stresses are between 0.4 – 16 MPa. That is one to almost three
741 orders of magnitude lower than measured in the mechanical data. Conversely, if
742 Eq. (6) were used to calculate the strain rate for the given T and d , with the
743 measured $\tau = 200 \text{ MPa}$, strain rates of 1×10^{-3} to $5 \times 10^{-2} \text{ s}^{-1}$ would result.

744 Our experimental samples contain higher wt.-% H_2O compared to the samples of
745 Rybacki and Dresen (2000), which is likely to have a marked effect on the rate of
746 DPC. Nonetheless, despite some uncertainties in the application of the RD00 flow
747 law, the results are expected to yield values within the expected order of
748 magnitude for DPC. The calculated stresses for the shear bands thus suggest that
749 the elevated bulk sample strengths of $\tau \approx 200 \text{ MPa}$ at the given bulk strain rate of
750 10^{-5} s^{-1} cannot be explained by representing the fine-grained material within shear
751 bands. Rather, an effect by a load-bearing framework of low strain lenses due to

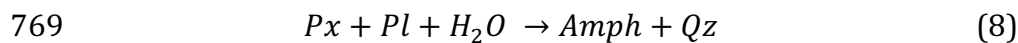
752 insufficient connectivity and unfavourable orientation of shear bands is suggested
753 to explain the observed bulk sample strengths. Bulk sample strength is interpreted
754 to be determined by the combined rate of DPC and GBS in the coarse-grained low
755 strain lenses and the fine-grained shear bands. The onset of DPC does not depend
756 on the occurrence of shear bands but because diffusion lengths are proportional to
757 the grain size, the rate of strain accommodation by DPC will vary strongly between
758 fine grained shear bands compared to low strain lenses which largely preserve the
759 coarse initial grain sizes. Delocalized viscous processes prior to shear band
760 formation are also indicated by the lower initial slope of the loading curve in the
761 mechanical data ([Figure 3a](#)), indicating a more viscous component of sample
762 deformation from the start of the experiment . DPC is speculated to cause this
763 viscous relaxation.

764

765 *4.2.3 The influence of strain on reaction rate as seen from the microstructure*

766 At 700 °C, fractures in Px porphyroclasts are extensively decorated by Amph
767 overgrowths ([Figure 6](#)), where Amph is forming by the reaction:

768



770

771 Amph is seen to grow along Px-internal fractures with no contacting boundary
772 towards Pl, indicating that element transport along the fractures occurred over
773 several μm distance. It is described in the literature that fracturing can lead to high
774 dislocation densities in the host crystal and is frequently associated with porosity
775 (e.g. Fitz Gerald et al., 1991; Fitz Gerald and Stünitz, 1993; de Ronde et al., 2005).
776 Fitz Gerald and Stünitz (1993) interpret from their observations that permeability
777 along the microfractures must have been greatly enhanced, allowing for solution
778 mass transport and mineral reactions along the fracture. Also from our
779 observations, there is a clear positive feedback between deformation and reaction.
780 This seems especially important in the 700 °C experiments, where the positive
781 contribution of deformation on reaction rate is seen more strongly in the
782 microstructure compared to 800 °C experiments. This is not unexpected, as
783 reaction and diffusion rates will increase with increasing temperature and the

784 rate-enhancing effects of deformation on reaction and diffusion may become less
785 important.

786

787 *4.3 Linkage to natural faults*

788 The findings from our experiments suggest that a transition from brittle to viscous
789 deformation in the studied mafic rock type initiates where solution-mass transport
790 processes occur at sufficiently high rates to accommodate deformation at the
791 imposed strain rate. No significant contribution of crystal plastic processes could
792 be observed. DPC and mineral reactions both take place simultaneously. The grain
793 size reduction is caused primarily by mineral reaction and nucleation of new
794 grains. The operation of DPC as a mechanism observed in our experiments
795 depends on the metastability of minerals in the starting material. This situation is
796 typical for most basalts and gabbros at amphibolite facies conditions and lower
797 temperatures.

798 For the continental crust, with its lower geothermal heat gradient compared to the
799 oceanic crust, mafic fault rocks at common strain rates ($< 10^{-9} \text{ s}^{-1}$) in the presence
800 of fluids are likely to go through their brittle-viscous transition at much lower
801 temperatures than observed in our experiments. Hydration reactions of feldspars
802 at e.g. greenschist facies conditions can lead to grain size reduction and phase
803 mixing, promoting viscous deformation by grain size sensitive creep mechanisms
804 (e.g. Fitz Gerald and Stünitz, 1993; Stünitz and Fitz Gerald, 1993).

805 In the oceanic crust, where confining pressures (i.e. lithostatic pressures) are much
806 lower for same temperatures compared to the continental crust, brittle-viscous
807 transitional behaviour is likely to occur at higher temperatures, i.e. similar
808 temperatures like in our experiments (e.g., Mehl and Hirth 2008). As pressures
809 generally are lower, fracturing is will be more common and is likely contributing to
810 deformation even to high temperatures.

811 As seen from our experiments, brittle-viscous transitional behaviour is not only a
812 function of the externally applied parameters such as P and T, but especially a
813 function of strain, i.e. microstructural evolution. This is an important factor to
814 consider, as typically rheology of rocks is modelled as a material property without
815 considering an evolution. We consider that this strain dependent rheology, as
816 observed in our experiments, can be extrapolated to natural fault systems. Where

817 the strain dependency of rheology bears the potential to lead to a ‘time-dependent’
818 brittle-viscous transition as microstructure evolves towards favouring viscous
819 deformation (as seen for the 700 °C experiments in our study).

820

821 **5. Summary and conclusions**

822 At the imposed experimental displacement rates, a transition from dominantly
823 brittle to brittle-viscous to dominantly viscous is observed between the
824 temperatures 600, 700 and 800 °C. The brittle-viscous transition in our study is
825 observed to occur via a switch from fracturing to diffusion creep (in the sense of
826 DPC) and grain boundary sliding as dominant viscous deformation mechanisms.
827 Viscous deformation in our experiments starts with the onset of diffusive mass
828 transport and starts to dominate the rheology when fine-grained, interconnected
829 zones have formed.

830 The important processes enabling viscous rheology are 1) efficient solution-mass
831 transport, 2) grain size refinement, which in our case as a result of reaction and
832 nucleation, and 3) shear band interconnection.

833 We observe a brittle-viscous transition not only as a result of increasing
834 temperatures but also via a microstructural evolution. Especially as the brittle-
835 viscous transition is approached in terms of temperature (in our case at 700 °C),
836 more evolved microstructure in shear bands allows for viscous deformation,
837 whereas low strain lenses still show largely brittle deformation. This leads to a
838 likely transient, mixed mechanical response of brittle and viscous rheology. For
839 constant syn-kinematic conditions (i.e. strain rate, P and T, fluid availability, etc.)
840 the syn-kinematic microstructural evolution with strain (and time) is expected to
841 change the relative importance of brittle and viscous deformation in favour of the
842 viscous processes.

843

844 **Acknowledgements**

845 We thank the team of the centre of nano imaging (SNI) at Basel University and Tom
846 Eilertsen at Tromsø University for help and assistance with the electron
847 microscopy. Terry Tullis is thanked for providing the Maryland Diabase material.
848 Willy Tschudin is thanked for excellent thin section preparation. We gratefully
849 acknowledge the funding provided by the Swiss National Foundation grant NF

850 200020_144448 and financial support from the Freiwillige Akademische
851 Gesellschaft, Basel, during the last stages of finishing this manuscript.

852

853

854 **References**

855

856 Ashby, M.F., Verrall, R.A., 1973. Diffusion-accommodated Flow and
857 Superplasticity. *Acta Metallurgica* 21.

858

859 Boullier, A.M., Geugen, Y., 1975. SP-Mylonites: Origin of Some Mylonites by
860 Superplastic Flow. *Contribution to Mineralogy and Petrology* 50, 93 – 104.

861

862 Brace, W.F., Kohlstedt, D.L., 1980. Limits of Lithospheric Stress Imposed by
863 Laboratory Experiments. *Journal of Geophysical Research* 85, 6248 – 6252.

864

865 Bukovská, Z., Jerábek, P., Morales, L.F.G., 2016. Major softening at brittle-ductile
866 transition due to interplay between chemical and deformation processes: An
867 insight from evolution of shear bands in the South Armorican Shear Zone.
868 *Journal of Geophysical Research* 121, 1158 – 1182.

869

870 Burov, E.B., 2011. Rheology and strength of the lithosphere. *Marine and*
871 *Petroleum Geology* 28, 1402–1443.

872

873 Byerlee, J., 1978. Friction of Rocks. *Pure and Applied Geophysics* 116, 615–626.

874

875 Byerlee, J.D., 1968. Brittle-ductile transition in rocks. *Journal of Geophysical*
876 *Research* 73, 4741 – 4750.

877

878 Byerlee, J.D., 1967. Frictional characteristics of granite under high confining
879 pressure. *Journal of Geophysical Research* 72, 3639 – 3648.

880

881 Bystricky, M., Mackwell, S., 2001. Creep of dry clinopyroxene aggregates. *Journal*
882 *of Geophysical Research* 106(B7), 13443 – 13454.

883

884 Carter, N.L., Tsenn, M.C., 1987. Flow properties of continental lithosphere.
885 *Tectonophysics* 136, 27 – 63.

886

887 Chen, S., Hiraga, T., Kohlstedt, D.L., 2006. Water weakening of clinopyroxene in
888 the dislocation creep regime. *Journal of Geophysical Research* 111, B08203.

889

890 Coble, R.L., 1963. A Model for Boundary Diffusion Controlled Creep in
891 Polycrystalline Materials. *Journal of Applied Physics* 34, 1679 – 1682.

892

893 de Ronde, A.A., Stunitz, H., Tullis, J., Heilbronner, R., 2005. Reaction-induced
894 weakening of plagioclase-olivine composites. *Tectonophysics* 409, 85 – 106.

895

896 Dimanov, A., Dresen, G., 2005. Rheology of synthetic anorthite-diopside
897 aggregates: Implications for ductile shear zones. *Journal of Geophysical Research*
898 110, B07203.
899

900 Dimanov, A.E., Rybacki, E., Wirth, R., Dresen, G., 2007. Creep and strain-
901 dependent microstructures of synthetic anorthite-diopside aggregates. *Journal*
902 *of Structural Geology* 29, 1049 – 1069.
903

904 Dimanov, A., Lavie, M.P., Dresen, G., Ingrin, J., Jaoul, O., 2003. Creep of
905 polycrystalline anorthite and diopside. *Journal of Geophysical Research* 108,
906 B001815.
907

908 Drury, M.R., Avé Lallemant, H.G., Pennock, G.M., Palasse, L.N., 2011. Crystal
909 preferred orientation in peridotite ultramylonites deformed by grain size
910 sensitive creep, Étang de Lers, Pyrenees, France. *Journal of Structural Geology*
911 33, 1776 – 1789.
912

913 Drury, M.R., Humphreys, F., 1988. Microstructural shear criteria associated with
914 grain-boundary sliding during ductile deformation. *Journal of Structural Geology*
915 10, 83 – 89.
916

917 Elliott, D., 1973. Diffusion Flow Laws in Metamorphic Rocks. *Geological Society of*
918 *America Bulletin* 84, 2645–2664.
919

920 Fitz Gerald, J.D., Boland, J.N., McLaren, A.C., Ord, A., Hobbs, B., 1991.
921 Microstructures in water-weakened single crystals of quartz. *Journal of*
922 *Geophysical Research* 96, 2139 – 2155.
923

924 Fitz Gerald, J.D., Stünitz, H., 1993. Deformation of Granitoids at low Metamorphic
925 Grade. 1. Reactions and Grain-size Reduction. *Tectonophysics* 221, 269–297.
926

927 Fossen, H., Tikoff, B., 1993. The deformation matrix for simultaneous simple
928 shearing, pure shearing and volume change, and its application to transpression-
929 transtension tectonics. *Journal of Structural Geology* 15, 413 – 422.
930

931 Fousseis, F., Handy, M.R., 2008. Micromechanisms of shear zone propagation at
932 the brittle–viscous transition. *Journal of Structural Geology* 30, 1242–1253.
933

934 Gerbi, C., Johnson, S.E., Shulman, D., Klepeis, K., 2016. Influence of microscale
935 weak zones on bulk strength. *Geochemistry Geophysics Geosystems* 17, 4064 –
936 4077.
937

938 Getsinger, A.J., Hirth, G., 2014. Amphibole fabric formation during diffusion creep
939 and the rheology of shear zones. *Geology* 42, 535 – 538.
940

941 Gifkins, R.C., 1976. Grain-Boundary Sliding and its Accommodation During Creep
942 and Superplasticity. *Metallurgical Transactions* 7A, 1225 – 1232.
943

944 Goldsby, D., Tullis, T.E., 2002. Low frictional strength of quartz rocks at
945 subseismic slip rates. *Geophysical Research Letters* 29, L015240.
946
947 Goncalves, P., Poilvet, J.-C., Oliot, E., Trap, P., 2016. How does shear zone
948 nucleate? An example from the Suretta nappe (Swiss Eastern Alps). *Journal of*
949 *Structural Geology* 86, 166 – 180.
950
951 Gratier, J.-P., Dysthe, D.K., Francois, R., 2013. The Role of Pressure Solution Creep
952 in the Ductility of the Earth's Upper Crust, in: Dmowska, R. (Ed.), *Advances in*
953 *Geophysics*. pp. 47 – 179.
954
955 Gratier, J.-P., Guiguet, R., Renard, F., Jenatton, L., Bernard, D., 2009. A pressure
956 solution creep law for quartz from indentation experiments. *Journal of*
957 *Geophysical Research* 114, B03403.
958
959 Gratier, J.-P., Richard, J., Renard, F., Mittempergher, S., Doan, M.-L., Di Toro, G.,
960 Hadizadeh, J., Boullier, A.-M., 2011. Aseismic sliding of active faults by pressure
961 solution creep: Evidence from the San Andreas Fault Observatory at Depth.
962 *Geology* 39, 1131–1134.
963
964 Green, H. W. II, Borch, R. S., 1989. A new molten salt cell for precision stress
965 measurements at high pressure. *Eur. J. Miner.* 1, 213 - 219.
966
967 Griggs, D.T., Turner, F.J., Heard, H.C., 1960. Deformation of rocks at 500 to 800°C.
968 *Geol. Soc. Am., Mem.* 79, 39 – 105.
969
970 Hacker, B.R., Christire, J.M., 1991. Experimental deformation of a glassy basalt.
971 *Tectonophysics* 200, 79 – 96.
972
973 Handin, J., 1966. Strength and ductility, in: Clark, S.P. (Ed.), *Handbook of Physical*
974 *Constants*, *Geol. Soc. Am. Mem.* pp. 223 – 289.
975
976 Hawthorne, F. C., Oberti, R., Harlow, G. E., Maresch, W. V., Martin, R. F.,
977 Schumacher, J. C., and Welch, M. D., 2012. Nomenclature of the amphibole
978 supergroup. *American Mineralogist* 97, 2031 – 2048
979
980 Heard, H.C., 1960. , in: Griggs, D.T., Handin, J. (Eds.), *Transition from Brittle*
981 *Fracture to Ductile Flow in Solnhofen Limestone as a Function of Temperature,*
982 *Confining Pressure and Interstitial Fluid Pressure, Rock Deformation, Mem. Geol.*
983 *Soc. Am. New York*, pp. 193 – 226.
984
985 Heilbronner, R., Barrett, S., 2014. *Image Analysis in Earth Sciences -*
986 *Microstructures and Textures of Earth Materials.* Springer-Verlag, Berlin.
987
988 Holyoke III, C.W., Kronenberg, A.K., 2010. Accurate differential stress
989 measurement using the molten salt cell and solid salt assemblies in the Griggs
990 apparatus with applications to strength, piezometers and rheology.
991 *Tectonophysics* 494, 17 – 31.

992 Janssen, C., Wirth, R., Rybacki, E., Naumann, R., Kemnitz, H., Wenk, H.-R., Dresen,
 993 G., 2010. Amorphous material in SAFOD core samples (San Andreas Fault):
 994 Evidence for crush-origin pseudotachylytes? *Geophysical Research Letters* 37,
 995 L01303.
 996
 997 Karato, S.-I., 2008. *Deformation of Earth Materials - an introduction to the*
 998 *rheology of solid earth*. Cambridge University Press, Cambridge.
 999
 1000 Keulen, N., Heilbronner, R., Stünitz, H., Boullier, A.-M., Ito, H., 2007. Grain size
 1001 distributions of fault rocks: A comparison between experimentally and naturally
 1002 deformed granitoids. *Journal of Structural Geology* 29, 1282 – 1300.
 1003
 1004 Kilian, R., Heilbronner, R., Stünitz, H., 2011. Quartz grain size reduction in a
 1005 granitoid rock and the transition from dislocation to diffusion creep. *Journal of*
 1006 *Structural Geology* 33, 1265–1284.
 1007
 1008 Kohlstedt, D.L., Evans, B., Mackwell, S.J., 1995. Strength of the Lithosphere:
 1009 Constraints imposed by laboratory experiments. *Journal of Geophysical Research*
 1010 100 (17), 517–587

 1011 Kohlstedt, D.L., Hansen, L.N., 2015. Constitutive equations, rheological behavior,
 1012 and viscosity of rocks, in: Schubert, G. (Ed.), *Treatise on Geophysics*. Elsevier,
 1013 Oxford, pp. 441 – 472.
 1014
 1015 Kronenberg, A.K., Shelton, G.L., 1980. Deformation microstructures in
 1016 experimentally deformed Maryland Diabase. *Journal of Structural Geology* 2, 341
 1017 – 353.
 1018
 1019 Mackwell, S.J., 1991. High-temperature creep of enstatite single crystals.
 1020 *Geophysical Research Letters* 18, 2027 – 2030.
 1021
 1022 Mancktelow, N.S., Pennacchioni, G., 2005. The control of precursor brittle
 1023 fracture and fluid–rock interaction on the development of single and paired
 1024 ductile shear zones. *Journal of Structural Geology* 27, 645 – 661.
 1025
 1026 Panozzo Heilbronner, R., 1984. Two-dimensional strain from the orientation of
 1027 lines in a plane. *Journal of Structural Geology* 6, 215 – 221.
 1028
 1029 Paterson, M.S., 2013. *Materials Science for Structural Geology*. Springer,
 1030 Dordrecht.
 1031
 1032 Paterson, M.S., Wong, T.-F., 2005. *Experimental Rock Deformation – The Brittle*
 1033 *Field*, 2nd ed. Springer, Berlin Heidelberg.
 1034
 1035 Pec, M., Stünitz, H., Heilbronner, R., Drury, M., 2016. Semi-brittle flow of granitoid
 1036 fault rocks in experiments. *Journal of Geophysical Research Solid Earth* 121,
 1037 B012513.
 1038

1039 Pec, M., Stünitz, H., Heilbronner, R., Drury, M., de Capitani, C., 2012. Origin of
1040 pseudotachylites in slow creep experiments. *Earth and Planetary Science Letters*
1041 355-356, 299 – 310.
1042
1043 Pennacchioni, G., Mancktelow, N., 2007. Nucleation and initial growth of a shear
1044 zone network within compositionally and structurally heterogeneous granitoids
1045 under amphibolite facies conditions. *Journal of Structural Geology* 29, 1757–
1046 1780.
1047
1048 Price, N.A., Johnson, S.E., Gerbi, C.C., West Jr., D.P., 2012. Identifying deformed
1049 pseudotachylyte and its influence on the strength and evolution of a crustal
1050 shear zone at the base of the seismogenic zone. *Tectonophysics* 518-521, 63 s
1051 518
1052
1053 Raterron, P., Jaoul, O., 1991. High-temperature deformation of diopside single
1054 crystal, 1. mechanical data. *Journal of Geophysical Research* 96, 14277 – 14286.
1055
1056 Richter, B., Stünitz, H., Heilbronner, R., 2016. Stresses and pressures at the
1057 quartz-to-coesite phase transformation in shear- deformation experiments.
1058 *Journal of Geophysical Research Solid Earth* 121, B013084.
1059
1060 Rutter, E.H., 1976. The kinetics of rock deformation by pressure solution.
1061 *Philosophical Transactions of the Royal Society of London* 283, 203 – 219.
1062
1063 Rutter, E.H., Peach, C.J., White, S.H., Johnston, D., 1985. Experimental
1064 “syntectonic” hydration of basalt. *Journal of Structural Geology* 7, 251 – 266.
1065
1066 Rybacki, E., Dresen, G., 2000. Dislocation and diffusion creep of synthetic
1067 anorthite aggregates. *Journal of Geophysical Research* 105, 26017 – 26036.
1068
1069 Rybacki, E., Gottschalk, M., Wirth, R., Dresen, G., 2006. Influence of water fugacity
1070 and activation volume on the flow properties of fine-grained anorthite
1071 aggregates. *Journal of Geophysical Research* 111, B03203.
1072
1073 Schmid, S., Panozzo, R., Bauer, S., 1987. Simple shear experiments on calcite
1074 rocks: rheology and microfabric. *Journal of Structural Geology* 9, 747 – 778.
1075
1076 Shelton, G., Tullis, J., Tullis, T., 1981. Experimental high temperature and high
1077 pressure faults. *Geophysical Research Letters* 8, 55 – 58.
1078
1079 Sibson, R.H., 1984. Roughness at the Base of the Seismogenic Zone: Contributing
1080 Factors. *Journal of Geophysical Research* 89, 5791 – 5799.
1081
1082 Sibson, R.H., 1982. Fault zone models, heat flow, and the depth distribution of
1083 earthquakes in the continental crust of the United States. *Bulletin of the*
1084 *Seismological Society of America* 72, 151 – 163.
1085
1086 Simpson, C., 1986. Fabric Development in Brittle-to-Ductile Shear Zones. *Pure*
1087 *and Applied Geophysics* 124, 269–288.

1088
1089 Stel, H., 1981. Crystal growth in cataclasites: Diagnostic microstructures and
1090 implications. *Tectonophysics* 78, 585 – 600.
1091
1092 Storti, F., Billi, A., Salvini, F., 2003. Particle size distributions in natural carbonate
1093 fault rocks: insights for non-self-similar cataclasis. *Earth and Planetary Science*
1094 *Letters* 206, 173 – 186.
1095
1096 Stünitz, H., Fitz Gerald, J.D., 1993. Deformation of granitoids at low metamorphic
1097 grade. II: Granular flow in albite-rich mylonites. *Tectonophysics* 221, 229 – 324.
1098
1099 Trepmann, C.A., Stöckert, B., 2003. Quartz microstructures developed during
1100 non-steady state plastic flow at rapidly decaying stress and strain rate. *Journal of*
1101 *Structural Geology* 25, 2035 – 2051.
1102
1103 Tullis, J., Yund, A., 1987. Transition from cataclastic flow to dislocation creep of
1104 feldspar: Mechanisms and microstructures. *Geology* 15, 606 – 609.
1105
1106 Tullis, J., Yund, R.A., 1977. Experimental deformation of dry Westerly granite.
1107 *Journal of Geophysical Research* 82, 5705 – 5718.
1108
1109 Yund, R.A., Blanpied, M.L., Tullis, T.E., Weeks, J.D., 1990. Amorphous material in
1110 high strain experimental fault gauges. *Journal of Geophysical Research* 95, 15589
1111 – 15602.
1112
1113
1114
1115
1116
1117
1118
1119

1120 **Figure Captions**

1121

1122 **Figure 1** : Sample assembly. a) Schematic cross-section of sample assembly. Inset
1123 shows details on sample. b) Thin section of sample 449 after deformation. Black
1124 arrow indicates unloading crack. FB = forcing block, SZ = shear zone.

1125

1126 **Figure 2** : Reference frame and definitions. a) Micrographs are oriented with the
1127 shear zone boundaries parallel to the x-direction with a dextral sense of shear. b)
1128 In rose diagrams, preferred orientations are marked with black dots; θ = angle
1129 between orientation and applied load (σ_1 direction); Φ = angle between
1130 orientation and shear plane (shear zone boundaries). c) Stresses are plotted as
1131 shear stress τ versus apparent shear strain γ_a , see Appendix. Stages of the
1132 experiment are indicated.

1133

1134 **Figure 3** : Mechanical data. a) Shear stress vs. apparent shear strain for
1135 experiments performed at $T = 600, 700$ and 800 °C, using confining pressures
1136 (P_c) of $\sim 0.5, 1.0$ and 1.5 GPa. Shear strain rate for all experiments is $\sim 3 \times 10^{-5} s^{-1}$. b) Mohr diagrams for same experiments. σ_3 = confining pressure; σ_1 = yield
1138 stress. (black lines) or quasi-steady state (grey dotted lines). In red, apparent
1139 friction coefficient μ' and angle of internal friction. μ' values decrease with
1140 increasing T and increasing P_c . Stress values usually stay below Byerlees
1141 relationship except for 600 and 700 °C experiments at $P_c = 0.5$ GPa.

1142

1143 **Figure 4** : Derivation of stress exponents. a) Shear stress vs. apparent shear strain
1144 rate, with calculated stress exponent n ; slope of linear fit is $1/n$. b) Different stress
1145 exponents calculated for different data-correction routines shown for two
1146 experiments performed at $T = 800$ °C / $P_c = 1.0$ GPa and $T = 300$ °C / $P_c = 0.5$ GPa.
1147 R16 = after Richter et al., 2016; H&K10 = after Holyoke & Kronenberg, 2010; P12=
1148 after Pec et al, 2012 (see Methods).

1149

1150 **Figure 5** : Microstructure development across the brittle-viscous transition.
1151 Experimental conditions are indicated, dextral shear sense applies to all. a) and
1152 b) At $T = 600$ °C, fracturing is extensive; a foliation (S) is developed by cataclastic

1153 flow; shear displacement is accommodated along shear bands and shear
1154 fractures in Riedel shear (R) orientations. c) Pore trails along fractures indicate
1155 partial healing. d) and e) At T=700 °C, fracturing is extensive in Px
1156 porphyroclasts; a foliation (S) is developed partly by cataclastic flow. e) Shear
1157 bands are recognized by a fine-scale compositional layering and intense grain
1158 size reduction; hydrous reaction products Amph and Zo are beginning to form. f)
1159 and g) At T = 800 °C, broad shear bands (white stippled lines) anastomose
1160 around low strain lenses; they are characterized by grain size reduction and the
1161 formation of a foliation parallel to the shear band boundaries; hydrous reactions
1162 products Amph and (to a lower extent) Zo are formed.

1163

1164 **Figure 6 :** Hydrous reactions at 700 °C. Left: digitally produced phase maps,
1165 right, BSE image of the same area. Dark grey = Pl; orange = Amph; bright grey =
1166 Px ; sample deformed at T = 700 °C, Pc = 1.0 GPa. Amph follows zones of high
1167 strain such as shear bands, or fractures within Px clasts.

1168

1169 **Figure 7 :** Shear band morphology as a function of temperature. Shear bands
1170 and shear fractures are traced in red. Light background layer are BSE contrast
1171 images of the shear zones. Rose diagrams (surface ODFs) show orientation of
1172 boundary segments of the traced structures. Horizontal shear bands developed
1173 at the forcing block-shear zone interface are omitted from the analysis. Rose
1174 diagrams show the dominance of more shear zone parallel shear bands at higher
1175 experimental T. b) Shear band width distributions. Shear bands stay largely
1176 below 10 µm at 600 °C, and get broader at higher T, reaching up to 70 µm for the
1177 presented 800 °C experiment.

1178

1179 **Figure 8 :** Micro- to nanostructures of shear bands developed at 600 °C. a) SEM
1180 BSE image of a shear band formed in the sample near interface with the forcing
1181 block; shear sense is dextral. b) - d) TEM images of a shear band similar to the
1182 one shown in a). Kinematic reference frame for images b) - d) is given in upper
1183 right corner in b). b) BF TEM image. Increasing grain size refinement from top to
1184 lower half of the image; cryst = crystalline; amor = amorphous. Note few
1185 remaining crystals (darker) within amorphous layers. c) HAADF (left) and BF

1186 TEM image (right) of nano-crystals mainly formed by Px; amorphous layers
1187 correlate with the typical darker grey-value of Pl. d) High-resolution BF image
1188 from a central part of the shear band; nano-crystalline layer enclosed between
1189 amorphous domains. White squares denote areas where diffraction spots are
1190 detected in FFT analyses (see Methods); locally, amorphous layers contain nano-
1191 crystals, identified both from diffraction spots in FFT images and from their dark
1192 appearance in the BF image.

1193

1194 **Figure 9** : Micro- to nanostructures of shear bands developed at 700 °C. a) SEM
1195 BSE image of a shear band. b) SE SEM image of the surface of a shear band;
1196 mostly Pl grains are visible; white arrow indicates shear direction, with top to
1197 the upper right. c) HAADF image showing a Px porphyroclast adjacent to a fine
1198 grained shear band formed by Pl + Amph; the Px porphyroclast shows a thin
1199 reaction corona of Amph; black arrow points to porosity within the Px clast. d)
1200 HAADF image of a Pl porphyroclast with surrounding fine-grained Pl in a shear
1201 band; the trace of an EDS profile is marked. Kinematic reference frame is the
1202 same as in c). e) Element counts of Si, Ca and Al (normalized to max. count value
1203 of the respective element) versus distance (pixel) along the profile marked in d);
1204 mean values (blue) are indicated for the porphyroclast and the Pl of the shear
1205 band.

1206

1207 **Figure 10** : Micro- to nanostructures of shear bands developed at 800 °C. a) SE
1208 BSE image of a shear band with typical compositional layering of Pl dominated
1209 layers alternating with Amph+Qz(+Pl) mixed layers. b) BF TEM image of Pl
1210 grains within a shear band; grains show a low defect density; porosity is low and
1211 grain boundaries are tight. c) HAADF image showing the typical compositional
1212 layering of Pl dominated layers alternating with Amph+Qz aggregates. d) BF-
1213 STEM image of the same area as in c).

1214

1215 **Figure 11** : Shape of plagioclase grains in shear bands at 800 ° C. a) BF TEM
1216 image of diamond-shaped Pl grains with a weak shape preferred orientation. b)
1217 Rose diagram (surface ODF) of Pl grain boundaries preferentially oriented at Φ
1218 = 10-30° . The ODF shows a weak anisotropy consistent with the dextral sense

1219 of shear. c) Grain boundary segments are visualized separately for horizontal (-
1220 $30^\circ < \Phi < 30^\circ$) and vertical ($30^\circ < \Phi < 150^\circ$) orientations (marked black in rose
1221 diagrams).

1222

1223 **Figure 12** : Grain size distribution of plagioclase in shear bands. a) Sample 416
1224 deformed at $T = 700^\circ\text{C}$, $P_c = 1.0\text{ GPa}$; area equivalent grain diameters, d_{equ} , were
1225 determined from SE images as shown in Fig. 9b. b) Sample 414 deformed at $T =$
1226 800°C , $P_c = 1.0\text{ GPa}$; area equivalent grain diameters, d_{equ} , were determined
1227 from TEM images of the FIB-foil shown in Fig. 10. Dark grey bars represent
1228 $>80\%$ of all grains; black line = kernel density estimate fit, number of grains, n ,
1229 and mode of curve fit are indicated.

1230

1231 **Figure 13** : Evolution of shear bands with increasing strain. a) Central parts of
1232 shear zones deformed at $T = 800^\circ\text{C}$ and $P_c = 1.0\text{ GPa}$ to increasing apparent
1233 shear strains; sample 449 ($P_c = 1.5\text{ GPa}$) is included for comparison. Shear bands
1234 are shown in orange; rose diagrams with surface ODF of shear band boundary
1235 segments on right. With increasing strain, dominant shear band orientation
1236 becomes more shear zone parallel and shear bands become wider and better
1237 interconnected. b) Stress - strain curves for samples shown in a). c) Increase of
1238 area fraction of shear bands with increasing shear strain. Although geometry of
1239 shear bands at 1.0 and 1.5 GPa differ, their area-% is identical..

1240

1241 **Figure 14** : Zones of initial shear localization. BSE SEM image of sample 460
1242 deformed at $T = 800^\circ\text{C}$, $P_c = 1.0\text{ GPa}$. Black arrows point to minute segregation
1243 of melt; nucleation of new Amph (white arrow) and Pl grains is observed.

1244

1245 **Figure 15** : Comparison of shear band orientation formed at peak stress (left)
1246 and at higher strains at quasi steady state. Rose diagrams are surface ODFs of
1247 shear zone boundary segments. Initiation of shear band shows comparable
1248 preferred angles for all temperatures. At higher temperatures however, shear
1249 band orientations are more shear zone parallel with increasing strain, i.e.
1250 microstructural evolution.

1251

1252 **Table 1** : Composition of Maryland Diabase starting material. EDS
1253 measurements as oxide wt.-% and calculated to stoichiometric mineral formula.
1254

1255 **Table 2** : List of experiments and experimental conditions.

1256 T = Temperature

1257 Pc = Confining pressure, averaged between $\gamma_a = 1.5$ to end of experiment;

1258 (*) denotes peak stress experiments where average Pc is calculated between
1259 beginning and end of experiment.

1260 Peak τ = Maximum shear stress.

1261 Flow τ = Shear stress during quasi-steady state or at end of experiment.

1262 γ_a = Total apparent shear strain.

1263 $\dot{\gamma}_a$ = Apparent shear strain rate: (1) constant displacement rate

1264 experiments. $\dot{\gamma}_a$ calculated as the average value between $\gamma_a = 1.5$ and end

1265 of experiment; (2) displacement rate stepping tests. $\dot{\gamma}_a$ as average value

1266 for each setting.

1267

1268 **Appendix Figure 1** : General shear setup within initial state and shear zone

1269 thickness, th0, and state at end of experiment and final shear zone thickness, thF.

1270 For representation purposes, the displacement is displayed to occur asymmetric

1271 by shift of only the upper forcing block.

1272 **Appendix Table 1** : Different measures for shear strain.

1273 th0 = estimated shear zone thickness at start of experiment (Appendix Figure 2).

1274 thF = measured shear zone thickness at end of experiment (Appendix Figure 1).

1275 d = axial displacement of σ_1 -piston.

1276 sdF = displacement of σ_1 -piston parallel to shear zone boundary (Appendix
1277 Figure 1).

1278 $k = th0/thF$ = pure shear component.

1279 $thF/th0$ (%) = relative thickness of sample after deformation.

1280 Γ_{eff} = effective shear strain (Appendix Eq. (A4)).

1281 γ_{TH} = shear strain determined from relative displacement of forcing blocks as
1282 measured on thin sections.

1283 γ_{comp} = simple shear component (Appendix Eq. (A5)).
 1284 γ_{a} = apparent shear strain (Appendix Eq. (A2)).
 1285 R_f = aspect ratio of finite strain ellipse (after Fossen & Tikoff, 1973).
 1286 ϕ = orientation of finite stretching direction (after Fossen and Tikoff, 1973).
 1287 ε_{m} = strain magnitude (Appendix Eq. (A6)).

1288
 1289

1290 **Appendix**

1291 *A1. Derivation of shear strains*

1292 General shear experiments like the ones described in this paper often experience
 1293 sample thinning, even if the samples are pre-compacted or annealed before the
 1294 actual start of the shear deformation. Thinning continues throughout the
 1295 experiments, as inferred from samples deformed under identical conditions to
 1296 different total strains. It is usually observed that the sample material does not
 1297 escape sideways. The strain is therefore taken to be plane strain and calculations
 1298 are made in 2 dimensions by assuming a combination of pure shear (thinning of
 1299 shear zone) and simple shear (displacement parallel to the piston-sample
 1300 interface).

1301 Measurements indicate that the samples thin linearly from the beginning of the
 1302 experiment to the end. Correlating the shear zone thickness, thF , with the axial
 1303 displacement, d , a linear trend of shear zone thinning is evident ([Appendix Figure](#)
 1304 [1](#)). The initial thickness, i.e., the thickness of the compacted samples at the start of
 1305 the experiment, depends on temperature. Two initial thicknesses for $T = 800^\circ\text{C}$ and
 1306 $T \leq 700^\circ\text{C}$ are derived ([Appendix Table 1](#)).

1307 For strain calculations, the axial displacement, d , of the σ_1 -piston is partitioned
 1308 into a shear component parallel to the 45° sample piston interface, and a thinning
 1309 component normal to the shear zone boundary. Dividing the total shear
 1310 displacement sdF , by the final thickness thF , γ_{TH} is derived ([Appendix Figure 2](#)).

1311

$$1312 \quad \gamma_{\text{TH}} = sdF / thF \quad (A1a)$$

$$1313 \quad sdF = (d - (th_0 - thF) \cdot \cos(45^\circ)) / \cos(45^\circ) \quad (A1b)$$

1314

1315 where: sdF : total displacement parallel to the piston-sample interface; $th0 / thF$:
 1316 initial / final thickness of sample.

1317 In this study, the shear strain is calculated from the experimental record as the
 1318 sum of individual increments of shear displacement divided by the instantaneous
 1319 shear zone thickness. The shear strain derived in this manner is referred to as
 1320 apparent shear strain γ_a :

1321

$$1322 \quad \gamma_a(k) = \sum_{i=2}^k \frac{sd(i) - sd(i-1)}{th(i)} \quad (A2)$$

1323

1324 $sd(i)$: displacement along piston-sample interface; $th(i)$: shear zone thickness at
 1325 time i . The shear strain values calculated in this fashion depend on the thinning of
 1326 the sample. γ_a is termed 'apparent', as it is not a real measure of simple shear.

1327 The pure shear component of the sample strain is calculated as

1328

$$1329 \quad k = th0 / thF \quad (A3)$$

1330

1331 Following Fossen and Tikoff (1993), the effective shear strain, Γ_{eff} , and the simple
 1332 shear strain component, γ_{comp} , are derived as

1333

$$1334 \quad \Gamma_{eff} = k^{-1} \cdot \tan(\psi) = sdF / th0 \quad (A4)$$

1335

$$1336 \quad \gamma_{comp} = \Gamma_{eff} \cdot \frac{2 \ln(k)}{k - k^{-1}} \quad (A5)$$

1337

1338 The difference between the strain measures is small as shown in [Appendix Figure](#)
 1339 [3](#). Note that, if $thF = th0$, i.e., if $k = 1$, all strain measures coincide: $\gamma_{TH} = \gamma_a = \Gamma =$
 1340 γ_{comp} . In order to be able to convert from axial to shearing experiments, the strain
 1341 magnitude is derived after Schmid et al. (1987):

1342

$$1343 \quad \varepsilon_m = \frac{1}{\sqrt{3}} [(\varepsilon_1 - \varepsilon_2)^2 + (\varepsilon_2 - \varepsilon_3)^2 + (\varepsilon_3 - \varepsilon_1)^2]^{1/2} \quad (A6)$$

1344

1345 where ε_m = strain magnitude; $\varepsilon_1, \varepsilon_2, \varepsilon_3$ = axes of the strain ellipsoid calculated
1346 after Fossen and Tikoff (1993). Plane strain conditions are assumed with $\varepsilon_2 = 1$.
1347
1348